

Deformation, strength and tectonic evolution of basal ice in Taylor Glacier, Antarctica

Sean Fitzsimons¹, Denis Samyn², and Regi Lorrain³

¹University of Otago

²Uppsala University

³Université Libre de Bruxelles

September 30, 2023

Abstract

Observation and measurements of ice structure and deformation made in tunnels excavated into the margin of Taylor Glacier reveal a complex, rapidly deforming basal ice sequence. Displacement measurements in the basal ice, which is at a temperature of -18°C , together with the occurrence of cavities and slickenslides, suggests that sliding occurs at structural discontinuities within the basal zone although we cannot rule out the possibility of rapid deformation in thin zones of high shear. Strain measurements show that the highest strain rates occur in ice with average debris concentrations of 26% followed by ice with debris concentrations of around 12%. The lowest strain rates occur in clean ice that has very low debris concentrations ($<0.02\%$). Deformation within the basal ice sequence is dominated by simple shear but disrupted by folding which results in shortening of the debris-bearing ice followed by attenuation of the folds due to progressive simple shear which generates predominantly laminar basal ice structures. About 60% of glacier surface velocity can be attributed to deformation within the 4.5 m thick sequence of basal ice that was monitored for this study, and 15% of motion can be attributed to sliding. The combination of high debris concentrations and high strain rates in the debris-bearing ice means that material transported in the basal ice is exposed to a high rates of abrasion which produces heavily striated and faceted clasts typical of temperate glaciers even though the basal ice is at a temperature of -18°C .

Hosted file

974491_0_art_file_11403912_s19k8t.docx available at <https://authorea.com/users/667576/articles/667756-deformation-strength-and-tectonic-evolution-of-basal-ice-in-taylor-glacier-antarctica>

1
2 **Deformation, strength and tectonic evolution of basal ice in Taylor Glacier,**
3 **Antarctica**
4

5 **Sean Fitzsimons¹, Denis Samyn², and Regi Lorrain³**

6
7 ¹School of Geography, University of Otago, P.O. Box 56, Dunedin, New Zealand.

8 <https://orcid.org/0000-0003-0513-7367>

9 ² Independent researcher, formerly at Laboratoire de Glaciologie, Faculté des Sciences,
10 Université Libre de Bruxelles, Belgium.

11 ³ Retired, Laboratoire de Glaciologie, Faculté des sciences, Université Libre de Bruxelles,
12 Belgium.

13
14 Corresponding author: Sean Fitzsimons (sean.fitzsimons@otago.ac.nz)

15 **Key Points:**

- 16 • Observations made in tunnels excavated in Taylor Glacier reveal a 4 m-thick basal ice
17 sequence
- 18 • Sliding or highly localized deformation in thin zones occurs at structural interfaces within
19 the basal ice
- 20 • About 60% of glacier surface velocity can be attributed to deformation within the 4.5 m
21 thick sequence of basal ice
22

23 Abstract

24 Observation and measurements of ice structure and deformation made in tunnels excavated into the
25 margin of Taylor Glacier reveal a complex, rapidly deforming basal ice sequence. Displacement
26 measurements in the basal ice, which is at a temperature of -18°C , together with the occurrence of cavities
27 and slickenslides, suggests that sliding occurs at structural discontinuities within the basal zone although
28 we cannot rule out the possibility of rapid deformation in thin zones of high shear. Strain measurements
29 show that the highest strain rates occur in ice with average debris concentrations of 26% followed by ice
30 with debris concentrations of around 12%. The lowest strain rates occur in clean ice that has very low
31 debris concentrations ($<0.02\%$). Deformation within the basal ice sequence is dominated by simple shear
32 but disrupted by folding which results in shortening of the debris-bearing ice followed by attenuation of
33 the folds due to progressive simple shear which generates predominantly laminar basal ice structures.
34 About 60% of glacier surface velocity can be attributed to deformation within the 4.5 m thick sequence of
35 basal ice that was monitored for this study, and 15% of motion can be attributed to sliding. The
36 combination of high debris concentrations and high strain rates in the debris-bearing ice means that
37 material transported in the basal ice is exposed to a high rates of abrasion which produces heavily striated
38 and faceted clasts typical of temperate glaciers even though the basal ice is at a temperature of -18°C .

39

40 1 Introduction

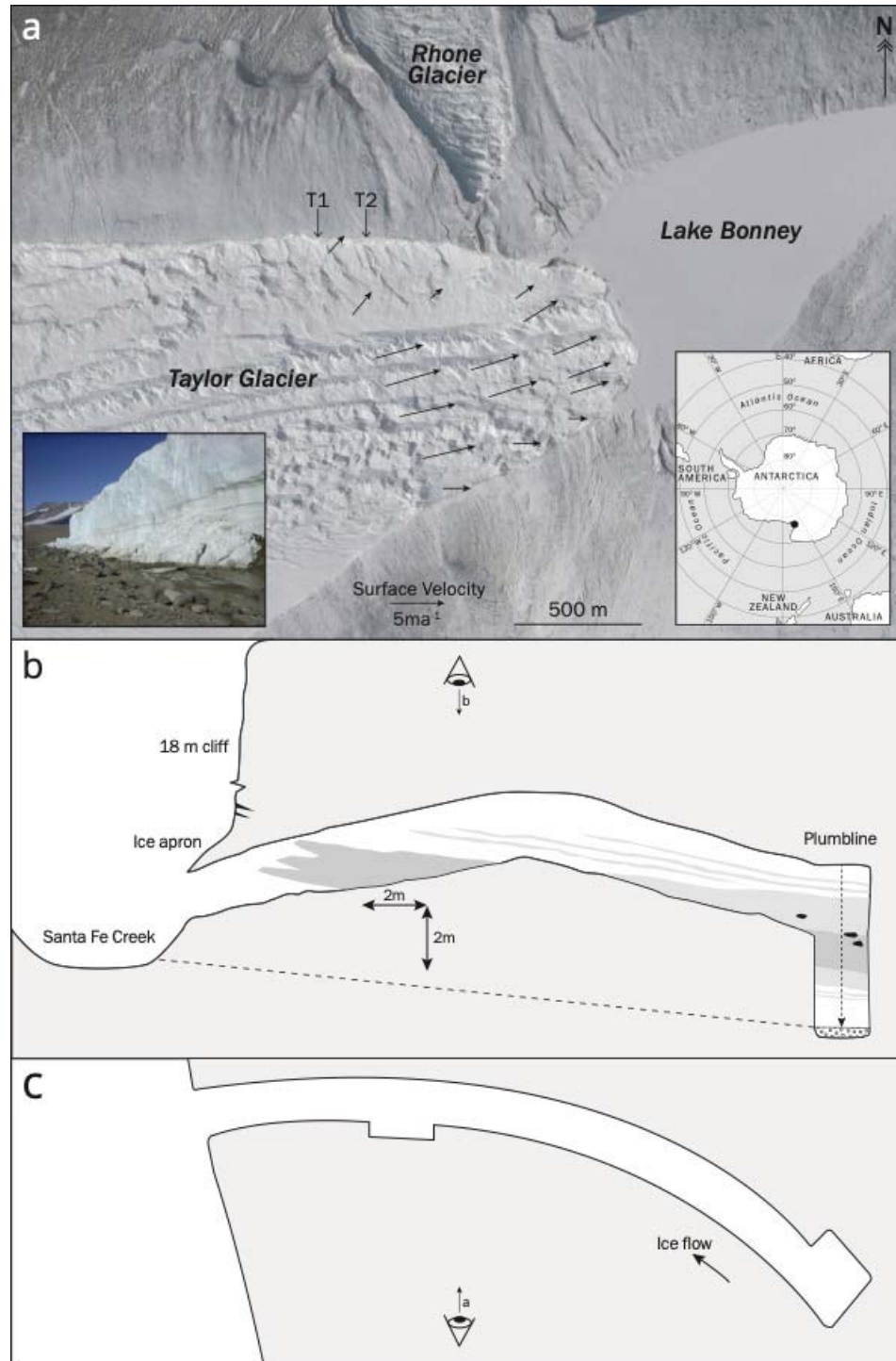
41 The most significant glacial processes occur at the beds of glaciers within a few metres of
42 the contact between ice and the glacier substrate. Deformation of ice and debris close in this zone
43 regulates the nature of motion at the bed, the rate of deformation experienced by ice and the
44 deformation and entrainment of subglacial sediment (Clarke, 2005; Hubbard, 2006; Iverson,
45 2010). One of the products of glacier-substrate interactions is basal ice which can be defined as
46 ice close to the bed of glaciers that has distinctive physical, chemical and mechanical properties
47 (Hubbard & Sharp, 1989; Hubbard et al., 2009). These properties are imparted by interactions
48 between glacier ice and the substrate. The processes that occur within basal ice and at glacier
49 beds underpin the large-scale behaviour of glaciers and control the geological processes at the
50 ice-substrate interface. These processes also determine the geological imprint of glaciation on the
51 Earth's surface (Alley et al., 1997; Boulton, 2006; Iverson, 2010).

52 Debris and solutes within basal ice alter the rheology of materials close to the bed which
53 has direct implications for glacier behaviour and glacial geological processes. For example, a
54 cold-based glacier with easily deformable basal ice will have higher surface velocities and a
55 thinner surface profile than a cold-based glacier without easily deformable ice (Pettit et al.,
56 2014). Both experimental and field-based research on the behaviour of ice/debris mixtures
57 suggests that we do not yet understand the constitutive properties of debris-ice mixtures (Moore,
58 2014; Thompson et al., 2020). There is a substantial body of experimental data that suggests the
59 addition of solid debris increases ice strength (Goughnor & Andersland, 1968; Nickling &
60 Bennett, 1984; Waller, 2001; Fitzsimons, 2006; Waller et al., 2012). However, field observations
61 remain equivocal (Moore, 2014). Some studies have determined that ice containing debris is
62 stronger than adjacent pure ice (Rabus and Echelmeyer, 1997; Fitzsimons et al., 1999, 2000,
63 2008; Fitzsimons & Howarth, 2020; Fitzsimons et al., 2023) whereas others have concluded that
64 ice containing debris is weakened relative to adjacent ice (Echelmeyer & Zhongxiang, 1987;
65 Cohen, 2000). Using compressive strength tests on ice from Taylor Glacier Lawson (1996)
66 showed that the addition of 10% debris by volume resulted in increases and decreases in ice

67 viscosity. Although some studies have concluded that the addition of debris has no impact on the
68 strength of the ice (Cuffey et al., 2000; Jacka et al., 2003; Moore, 2014) the general view is that
69 sediment in ice is expected to be stronger than adjacent ice and less susceptible to ductile
70 deformation well below the freezing point (Moore, 2014; Warbritton et al., 2020). In an
71 extensive review of the behaviour of frozen debris Moore (2014) concluded that ice-debris
72 mixtures are more resistant to deformation at low temperatures than pure ice but that at
73 temperatures closer to melting the growth of an interfacial water film can lead to profound
74 weakening. Collectively this work has demonstrated that there are several key gaps in our
75 understanding and the complexity of linkages between ice, debris, and glacier behaviour remains
76 elusive.

77 Taylor Glacier is an outlet glacier that flows from Taylor Dome which is part of the East
78 Antarctic Ice Sheet (Figure 1). The glacier terminates in the McMurdo Dry Valleys at the
79 permanently ice-covered Lake Bonney where the ice margin is characterized by 18-20 m high
80 cliffs. At the glacier terminus Robinson (1984) measured a mean ice surface temperature of
81 -17°C and concluded that the glacier was at the pressure melting point some distance upstream
82 of the terminus. Using an ice penetrating radar Hubbard et al. (2004) concluded that upstream of
83 the glacier terminus the bed consisted of saturated sediment or ponded liquid. Later work has
84 mapped widespread hypersaline groundwater that is connected to Blood Falls, a hypersaline
85 water discharge at the glacier terminus (Foley et al., 2016; Mikucki et al., 2015; Badgely et al.,
86 2017). Study of ice-crystal textures and gas content of the basal ice from Taylor Glacier show
87 that significant shearing has occurred within this basal ice (Samyn et al., 2005a) and inferred that
88 that variations in resistance to deformation occur at the cm to mm-scale within the basal ice.
89 Pettit et al. (2014) used a two-layer flowband model to investigate glacier behaviour and
90 concluded that the basal ice contributes 85-90% of glacier surface velocity and that the basal ice
91 was likely 10-15 m-thick and 20-40 times softer than Holocene age glacier ice. These findings
92 suggest that at least in some circumstances cold-based glaciers can be very sensitive to subglacial
93 deformation processes.

94 Here we hypothesize that strain in the basal zone of Taylor Glacier is localized to thin
95 bands of intense shear or sliding and that deformation of the basal ice is the major component of
96 glacier surface velocity. We further hypothesize that despite the low temperature at the margin of
97 this glacier localized shear and potentially sliding results in a structural evolution of the basal
98 zone and that these processes impart a distinctive glacial geological signature. This paper
99 describes the geomorphological setting and the methods used in the study (Section 2), and
100 presents observations of the composition and deformation of the basal zone from a combination
101 of field and laboratory analyses (Section 3). Interpretation of the data focuses on the patterns of
102 ice deformation, the rheological controls of deformation in the basal zone of the glacier, and the
103 geological imprint of these processes (Section 4).



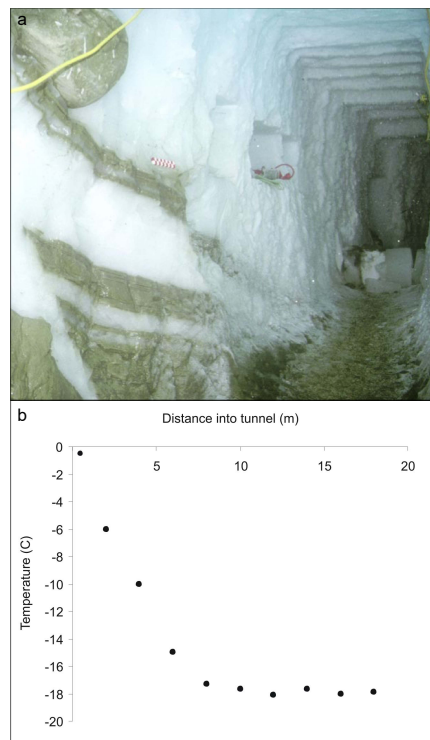
104

105 **Figure 1.** (a) Location map of Taylor Glacier showing the location of the tunnels (T1 and T2)
 106 and the velocity distribution over the terminus area. Base image: Google Earth, CNES/Airbus,
 107 image date: 22 November 2016. (b) and (c) Elevation and plan of the second tunnel excavated in
 108 1999.

109 **2 Data and methods**

110 2.1 Excavation

111 In the austral summer of 1998-1999 a 20 m-long tunnel was excavated approximately 1.1
 112 km upstream of the terminus at 77.71994°S 162.21939°E (T1 in Figure 1) using electric
 113 chainsaws with tungsten carbide cutters on the chain to make relief cuts in the ice, a demolition
 114 hammer to break up the ice and a sled to remove the ice from the tunnel. This tunnel was studied
 115 for a 2 week period but was destroyed by a combination of melting and flooding before it could
 116 be resurveyed the following summer. A second tunnel was excavated and instrumented in
 117 December 1999 approximately 200 m downstream of the first tunnel at 77.72068°S 162.22854°E
 118 (T2 in Figure 1). This tunnel was resurveyed in January 2000 and again in November 2000. The
 119 tunnelling process is documented in a series of short videos stored in Zenodo (Fitzsimons,
 120 2023). The temperature of the ice measured along the tunnel was $-18\pm 1^\circ\text{C}$ beyond 8 m of the
 121 tunnel entrance (Figure 2). The air temperature at the back of the tunnel remained around -15°C
 122 during excavation. Both tunnels were approximately 20 m-long and curved to avoid direct
 123 sunlight getting into the tunnels. The walls were oriented parallel to ice flow at the end of each
 124 tunnel. A 4 m-deep shaft was cut at the end of the second tunnel to expose the debris-bearing
 125 basal ice (Figure 3). Most of the observations and data reported in this paper come from the
 126 second tunnel.



127

128 **Figure 2.** (a) Entrance to the second tunnel after excavation showing basal debris layers rising
 129 toward the ice edge. The abrupt termination in the debris layers is the contact between the basal
 130 ice and the marginal ice apron. A 500 mm-diameter boulder rests on the top of the basal debris
 131 layer in the upper left corner of the photograph. (b) Temperature measured using thermocouples
 132 placed in holes drilled 200 mm into the tunnel wall from the entrance to the end of the tunnel.

133 2.2 Debris characteristics

134 The particle size distribution of sediments was determined by treating subsamples with 5
135 ml of 30% H₂O₂ to digest organic matter and rinsed in de-ionised water. Biogenic silica was
136 removed using 10 ml of 1 M NaOH and rinsed with de-ionised water. The samples were then
137 treated with 5 ml of 5% sodium hexametaphosphate solution and shaken gently for two hours to
138 deflocculate clay-sized particles. The treated samples were analysed using a Malvern Mastersizer
139 2000 laser particle size analyser or sieved if the samples contained particles >2 mm in diameter.

140 Debris concentration measurements were made by displacing the samples in water to
141 determine volume, then the sample was melted, the water evaporated and the remaining sediment
142 weighed. Debris concentration are expressed as percentages of volume calculated using a particle
143 density of 2700 kg.m⁻³.

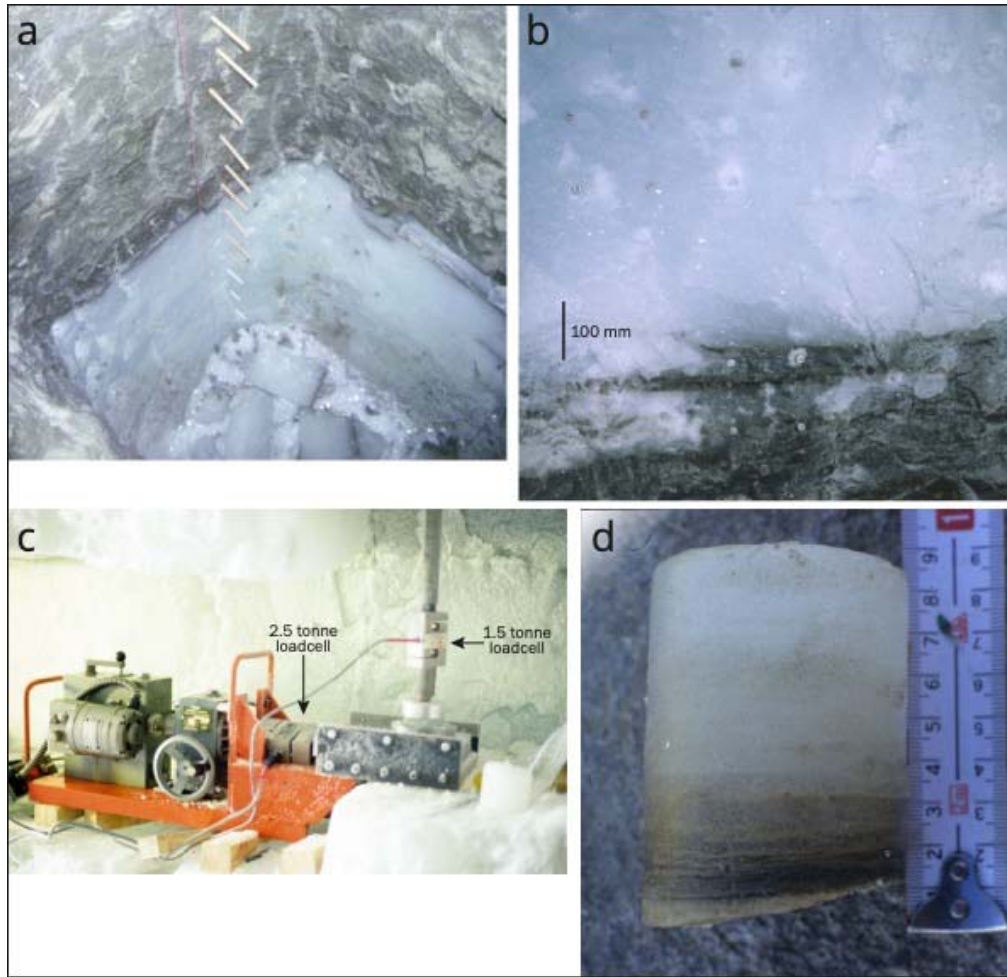
144 Three representative samples of 30 particles > 40 mm in diameter were retrieved by
145 melting blocks of the massive ice facies (section 4.1). These particles were examined for
146 striations and their shape was classified using Powers roundness classes (Powers, 1953).

147 2.3 Ice motion measurements

148 Measurements of ice movement were obtained using plumblines and engineers dial
149 gauges that were rock-bolted to boulders in the basal ice. The dial gauges used were Mitutoyo
150 series 2 gauges that have a precision of ± 0.02 mm and an accuracy of ± 20 μ m. The plumblines
151 consisted of nylon lines attached to a peg drilled and frozen into the top of the tunnel wall
152 (Figure 3a). The line was held taut with a plumb bob which was mounted above a brass target
153 drilled and frozen into the tunnel floor. Displacements were measured from the plumblines and
154 wooden markers drilled and frozen into the ice at 100 mm intervals using a digital caliper for
155 displacements up to 200 mm and a steel tape for displacements >200 mm. The plumblines were
156 resurveyed at intervals of 27, 42 and 403 days between December 1999 and November 2000.
157 Although the motion of brass target on the floor were measured and appeared to be stationary,
158 we cannot entirely discount the possibility that it is moving.

159 2.4 Strain measurements

160 Ice strain was measured using strain arrays that consisted of square arrays of stainless
161 coach screws that were drilled and frozen into the tunnels walls parallel to the ice flow (Figure
162 3b). Each stainless steel coach screw had a cone milled into its head in order to accurately
163 position a digital caliper that had locating cones fixed to the jaws. Measurements were made
164 using a Mitutoyo digital caliper with a precision of 0.001 mm. The caliper was calibrated by
165 repeat measurements of cones milled into a block of stainless steel. Repeated measurements of
166 the calibration block resulted in an operator error of ± 0.0096 mm and an accuracy of ± 0.02
167 (n=60). All the strain rates reported in this paper are based on measurements between 42 and 403
168 days. During this time, some bulging of the tunnel walls occurred, which could introduce errors
169 related to differences in closure rates in different basal ice facies. This problem is addressed in
170 section 2.7 of this paper. Bulging the the tunnel walls were monitored by surveying the shape of
171 the tunnel over time



172

173 **Figure 3.** Monitoring ice deformation. (a) Plumblines and wooden pegs in the shaft excavated at
 174 the end of the tunnel. (b) Strain arrays of four stainless steel coach screws in the upper left and
 175 lower centre, located at the interface between debris bearing and clean ice. (c) Direct shear
 176 device used for *in situ* strength tests. At left is a Wykeham Farrance direct shear machine with a
 177 2.5 tonne load cell between the stepper motor and the moving stainless steel plate. The vertical
 178 load is applied by a truck pneumatic shock absorber (out of view on the top of the vertical pole)
 179 separated from the top of the sample with a 1.5 tonne load cell. (d) Stratified debris-bearing ice
 180 sample tested in the direct shear device.

181 Strain rates were calculated from the corners of triangles defined from the strain arrays
 182 using a numerical calculation of a Mohr circle based on the method of Ramsay (1967) and used
 183 in glaciology by Hambrey and Müller (1978) and Hambrey et al. (1980). We have followed the
 184 convention for principal strain rates that $\dot{\epsilon}_1$ and $\dot{\epsilon}_3$ are horizontal, that $\dot{\epsilon}_1 \geq \dot{\epsilon}_3$, that extension is
 185 positive, and that $\dot{\epsilon}_3$ is always vertical (Sharp et al., 1988). Shear strain rate was calculated as:
 186 $\dot{\gamma} = \frac{\dot{\epsilon}_1 - \dot{\epsilon}_2}{2}$. The analytical techniques and errors associated with the strain calculations derived
 187 from field measurements made in tunnels are described in Fitzsimons et al. (2008). If the walls of
 188 the tunnel did not bulge $\dot{\epsilon}_3$ would equal zero, which is not the case with any of the measurements.
 189 However, $\dot{\epsilon}_3$ is an order of magnitude less than $\dot{\epsilon}_1$ and both $\dot{\epsilon}_1$ and $\dot{\gamma}$ increase into the tunnel so

190 we conclude that tunnel closure has not introduced major errors into the calculation of strain
191 rates. $\dot{\epsilon}_2$

192 2.5 Ice sampling

193 Samples of basal ice were collected for chemical and structural analysis using a chainsaw
194 in ice with relatively low debris concentrations and a 59 mm diameter diamond corer where the
195 ice contained high debris concentrations or larger particles. Following collection, the frozen
196 samples were returned to the laboratory where they were subsampled in a freezer using a band
197 saw to produce samples of about 50 ml. After subsampling, the ice was melted at room
198 temperature within 10 min. of being cut and immediately filtered with 0.45 μm cellulose nitrate
199 filter paper. The laboratory procedure is described in Fitzsimons et al. (2008).

200 2.6 Direct shear tests

201 A series of direct shear tests were undertaken in the tunnel using a modified laboratory
202 direct shear device (Figure 3c). The shear box was constructed on stainless steel plates that were
203 drilled to accommodate a 59 mm diameter cylindrical sample (Figure 3d) and driven by a stepper
204 motor through a load cell to move the upper plate (Figure 3c). The device was capable of
205 displacing the sample by about 5 mm which is a strain of approximately 8%. Shear test samples
206 were cut from the basal ice using a diamond corer driven by an electric drill. The experiments
207 were conducted in the tunnel which had an air temperature of -15°C , with displacement rates of
208 0.85 mm.h^{-1} and a normal load of 200 kPa. The normal load was applied by a pneumatic truck
209 shock absorber attached to the tunnel roof and a load cell above the sample (Figure 3c). The tests
210 were run for 3 to 4 hours to reach peak shear strength.

211 2.7 Limitations

212 Making ice deformation measurements in tunnels is problematic because any instruments
213 introduced into the glacier bed run the risk of changing the boundary conditions that they are
214 designed to measure. This is particularly the case with tunnels cut into glacier margins because
215 the ice will tend to creep into the tunnel. In this study we have attempted to mitigate the effects
216 of creep of the tunnel walls from the strain measurements by a combination of orienting the
217 planes in which measurements were made parallel to ice flow, and by simultaneously recording
218 deformation of the tunnel walls. Although the presence of the tunnel has changed the strain
219 behaviour of the ice, the measurements we made are consistent with the results of the direct
220 shear tests which leads us to conclude that the measurements we have made capture the relative
221 differences between the three main ice facies and sub-facies that were present at Taylor Glacier
222 described in section 4, below.

223 3 Results

224 3.1 Physical characteristics of the basal ice

225 Three distinctly different facies can be identified in the basal zone; clean englacial ice,
226 stratified ice that consists of two subfacies, and a coarse pebble-cobble gravel at the bottom of
227 the excavation (Table 1). The stratified facies consists of two subfacies: a laminated subfacies

228 composed of alternating laminae of debris-bearing and; clear clean ice layers 1 to 5mm thick and
 229 a massive subfacies that has an unstructured appearance.

230

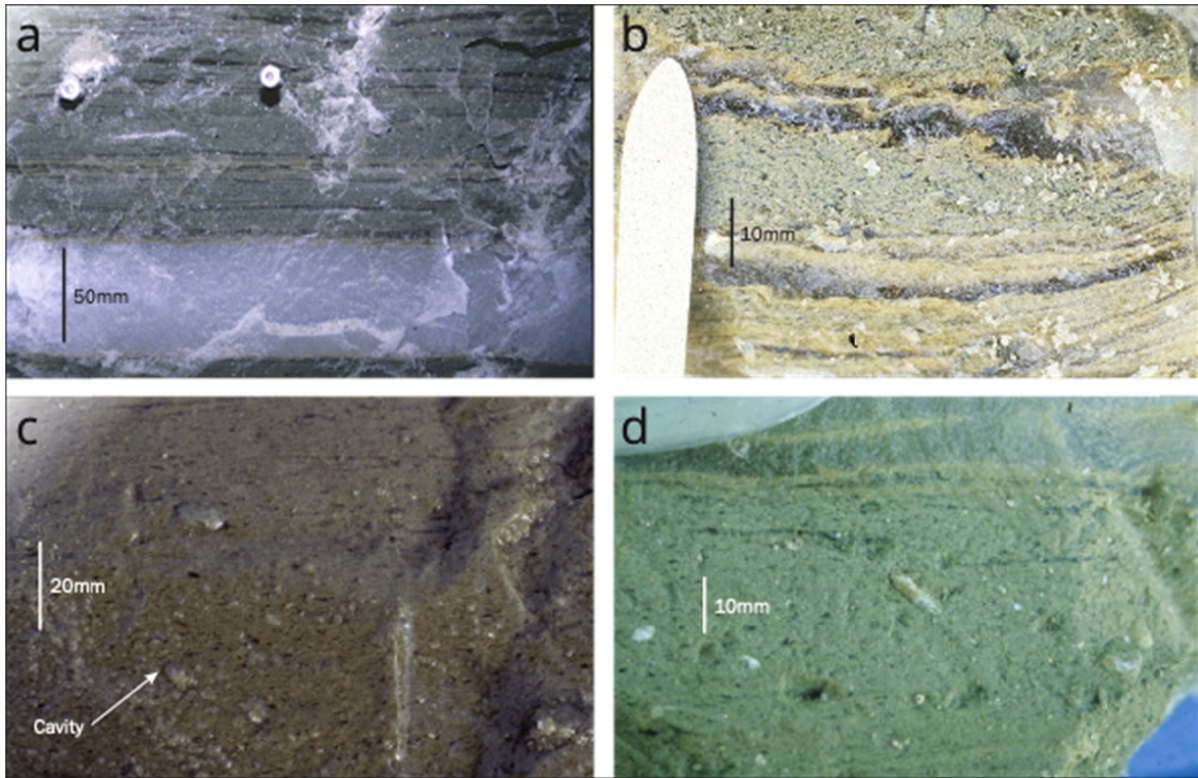
231 **Table 1**

232 Basal Ice Facies Characteristics
 233

Facies	Subfacies	Debris concentration [% vol.]		Physical characteristics
		Mean	s.d.	
Englacial		0.19	0.4	Bubbly white ice with very low debris concentrations.
Stratified	Laminated	21.0	15.6	Thin laminae of debris bearing ice alternating with laminae of clean, clear, bubble-free ice. Both laminae are <5 mm wide
	Massive	33.2	2.6	Debris bearing ice with massive (structureless) appearance. Wide range of particle sizes from boulders 1.5 m in diameter to silt-sized particles.
Gravel		65	-	Cobble and pebble gravel at the base of the excavation, ice confined to pore spaces.

234

235 The clean englacial ice consists white bubbly ice with very low debris concentrations that
 236 average 0.19% (Figure 3b, Table 1). The debris consists of dispersed silt to sand-sized particles
 237 and most of the stretched bubbles have axial ratios between 1:3 and 1:5. The laminated subfacies
 238 consists of finely laminated debris-rich ice and clean, clear ice layers (Figure 4a and 4b).
 239 Individual laminae range from 5 mm to less than 1 mm-thick and the debris ranges from
 240 abundant silt-sized particles up to boulder-sized particles held in the ice (Figure 2). The massive
 241 subfacies consists of densely-packed debris in a matrix of clear, clean ice. Although this ice has
 242 the appearance of being massive sections cut from the ice reveal the presence of abundant clear,
 243 clean ice lenses and laminae (Figure 4c and d). Average debris concentrations in this subfacies
 244 are 33.2 % vol. The very low standard deviation (2.6) reflects remarkably uniform debris
 245 concentrations in the central part of this subfacies (Table 1).



246

247 **Figure 4.** Basal ice facies exposed in the tunnel walls. (a) Laminated subfacies interbedded with
 248 the clean facies. The two bolts shown in the upper part of the photograph are part of a strain
 249 array. (b) Laminated subfacies with folded and sheared layers of clean bubble-free ice. (c)
 250 Massive facies with clear ice lenses and small pebble with stoss and lee-side cavities. (d)
 251 Massive facies with small pebbles. Ice flow is from right to left in all photographs.

252 The bottom of the shaft consisted of a 300 mm-thick coarse cobble-pebble gravel that
 253 stopped the excavation. Attempts to drill through the gravel with an ice auger equipped with
 254 tungsten carbide cutters and an attempt to map the geometry of the unit with a ground
 255 penetrating radar were unsuccessful.

256 Solute concentrations are highly variable in the basal ice (Table 2). The englacial ice is
 257 characterised by low concentrations in Cl^- and the major cations, and the values have a low
 258 standard deviation. The laminated subfacies is characterised by moderate concentrations of Cl^-
 259 and the major cations with a relatively high standard deviation likely reflecting two
 260 subpopulations of the clean clear laminae and the debris-bearing laminae. The highest solute
 261 concentrations were found in the massive subfacies where Cl^- is an order of magnitude greater
 262 than the laminated subfacies and the major cations are all at least three times the values of the
 263 laminate subfacies, with the exception of Na^+ which is lower than the value for the laminated
 264 subfacies (Table 2). The high standard deviation of the partial TDS measure shows that there
 265 is very high variability in the values in both stratified subfacies.

266

267

268 **Table 2**
 269 *Average Solute Concentrations for the Ice Facies*^a
 270

Facies (number of samples)	Cl ⁻	Na ⁺	Ca ²⁺	K ⁺	Mg ²⁺	TDS ^a	s.d.
Englacial (16)	0.28	0.41	0.55	0.03	0.04	1.31	0.68
Stratified laminated subfacies (21)	82.00	39.43	123.84	5.93	4.10	280.20	236.05
Stratified, massive subfacies (5)	1084.07	22.30	394.30	59.55	21.30	1581.53	1716.41

271 ^a Values in parts per thousand

272 ^b Partial measure of Total Dissolved Solids

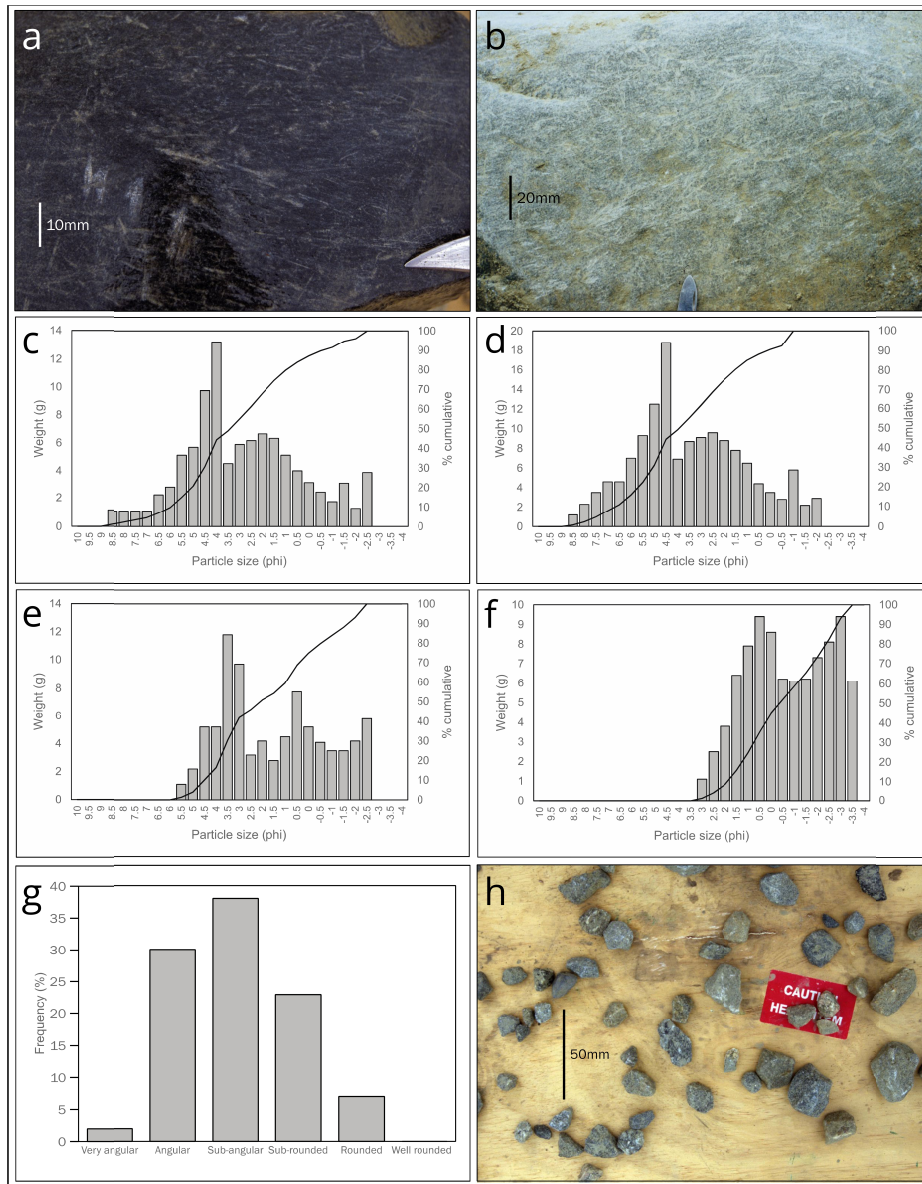
273

274 3.2 Sedimentology and structure

275 Both the laminated and massive subfacies contain dolerite, gneiss and granite boulders up
 276 to 600 mm in diameter (Figure 2). A selection of pebble to cobble-sized particles were recovered
 277 from the ice by allowing the ice matrix of samples to sublimate. These particles were frequently
 278 faceted and exhibited striae in cross cutting patterns with fine rock debris preserved adjacent to
 279 the striae (Figure 5a, b). Although not as well developed or abundant as striae on dolerite
 280 particles, gneiss and granite clasts also exhibited striae in cross-cutting directions, primarily on
 281 protuberances on the particles (Figure 5b). The cross-cutting striae suggests substantial rotation
 282 of the particles within the basal ice during abrasion. A few striated ventifacts were recovered
 283 from the laminated subfacies.

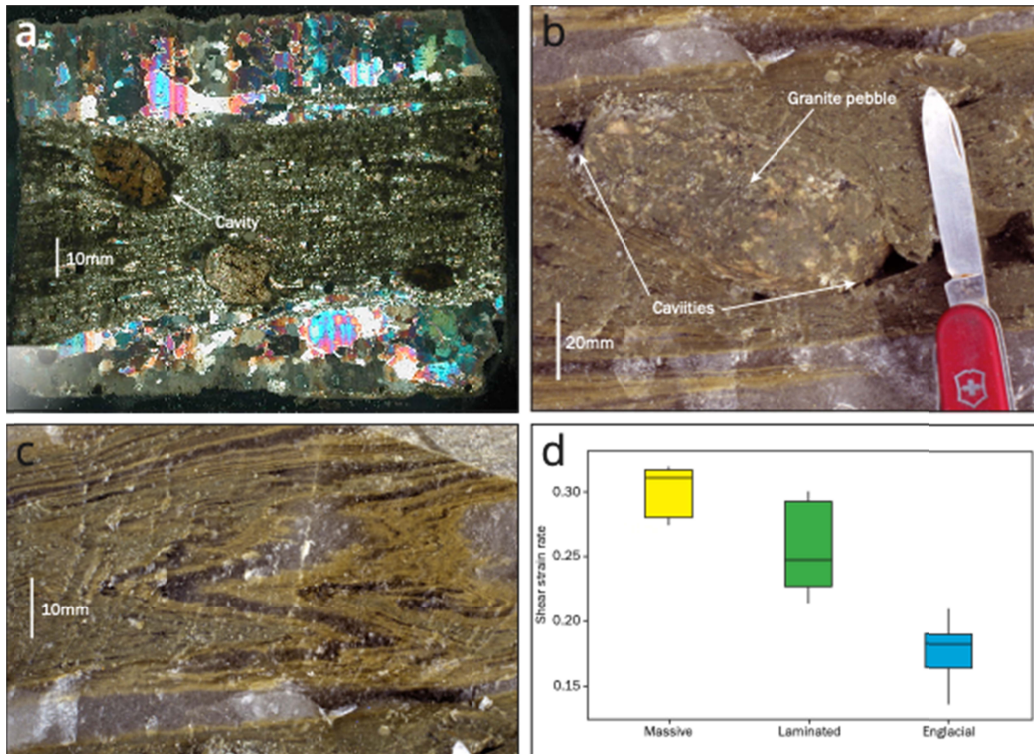
284 Particle size distributions of the sediment fractions less than 3.5 ϕ (11 mm) from the
 285 massive and laminated subfaces show that all the samples were very poorly sorted and
 286 characterized by multi modal distributions (Figure 5c, d and e). The largest peak in the
 287 distributions occurs between 3.5 and 4.0 ϕ (0.088 to 0.062 mm), which encompasses fine sand
 288 and coarse silt particles. A persistent secondary peak occurs at 2 ϕ (4 mm), which is composed
 289 of fine gravel particles. The modal particle shape is subangular but there are large numbers of
 290 subrounded and angular particles (Figure 5g and h).

291 Although the laminated and massive subfacies are dominated by planar structures (Figure
 292 6), numerous ductile deformation structures were observed, particularly in the laminated
 293 subfacies. Figure 6a shows a thin section of a layer of the laminated subfacies between two
 294 layers of englacial ice and there is a strong contrast in the diameter of ice crystals in the two
 295 facies. Two 10-15 mm diameter pebbles show that the ice layers are warped over the particles
 296 and that there are dark shadow zones on the stoss and lee sides of the pebbles, some of which are
 297 air-filled cavities.



300 **Figure 5.** Characteristics of debris in the basal ice and adjacent surficial sediments. (a)
 301 Randomly oriented striae on a polished dolerite clast (b) Randomly oriented striae on a gneiss
 302 clast. The striae appear “fresh” judged from the presence of powdered rock debris adjacent to
 303 striations. Both cobbles are from the top of the main debris band 3-3.5 m above the datum. (c)
 304 Particle size distribution from the center of the massive subfacies debris band 2.8 m above the
 305 shaft datum. (d) Particle size distribution from the top of the main debris band 3.4 m above the
 306 datum (e) Particle size distribution from the laminated subfacies facies 3.6 m above the datum.
 307 (f) Particle size distribution from the stream channel adjacent to the ice margin. (g) Roundness of
 308 pebbles from the main debris band classified using Powers roundness classes (Powers, 1953). (h)
 309 Predominantly subangular pebble-sized particles retrieved from melting 10kg of ice from the
 310 massive subfacies 3 m above the datum.
 311

312



313

314 **Figure 6.** Deformation structures in the laminated subfacies. (a) Thin section under polarized
 315 light showing clean ice above and below a layer of the laminated subfacies. Ice crystals in the
 316 debris-bearing ice are less than 1 mm in diameter and the clean ice has crystals 5-10 mm in
 317 diameter. (b) Prolate-shaped particle in the debris-bearing ice with characteristic stoss and lee-
 318 side air filled cavities. (c) A tight polyharmonic recumbent fold with multiple shear bands
 319 extending into the overlying ice. (d) Box and whisker plot of the shear strain rate showing
 320 median, upper quartile ranges and the maximum and minimum values. The ice flow is from right
 321 to left in all photographs.

322 3.3 Strength of the basal ice

323 The direct shear tests show that the clean ice has the highest shear strength, followed by
324 the laminated subfacies and the massive subfacies (Table 3). The massive subfacies has half the
325 average shear strength of the englacial samples. The average peak shear strength of the samples
326 from the different facies are significantly different from each other (t-tests with p values between
327 0.000 and 0.008) and the tests have low standard deviations. The shear strain rate calculated from
328 the strain arrays shows that the materials with the highest strength, the englacial facies, have the
329 lowest strain rates and the lowest strength materials, the massive subfacies, have the highest
330 shear strain rates (Table 3). A few triaxial tests using samples cut so that the layers are 45° to the
331 long axis of the samples were undertaken in laboratory conditions. Although fewer in number,
332 the results of these test are in the same order as the direct shear tests conducted in the field
333 shown in Table 3. While some of these tests of resulted in barrel-shaped failures of the samples
334 many failed along ice layers within the laminated facies (Fig. 7).

335



336

337 **Figure 7.** Result of a triaxial test of a sample of the laminated subfacies showing failure
338 localized to an ice-rich layer in the laminated subfacies. This test was undertaken with the
339 sample in an air-filled pressure vessel maintained at 200kPa and -18°C for the duration of the 12
340 hr test.

341

342

343 **Table 3**344 *Peak Shear Strength Values for Ice from the Basal Zone of Taylor Glacier*

345

Facies	Number of samples	Shear strength (MPa) ^a		Shear strain ^b
		Mean	s.d.	
Englacial	3	1.21	0.01	0.177
Laminated subfacies	5	0.91	0.11	0.257
Massive subfacies	4	0.64	0.01	0.301

346 ^a Mean peak shear strength from direct shear tests from direct shear tests done in the tunnel and
 347 their standard deviations.

348 ^b Shear strain rate $\dot{\gamma} = \frac{\epsilon_1 - \epsilon_2}{2}$, see section 2.4.

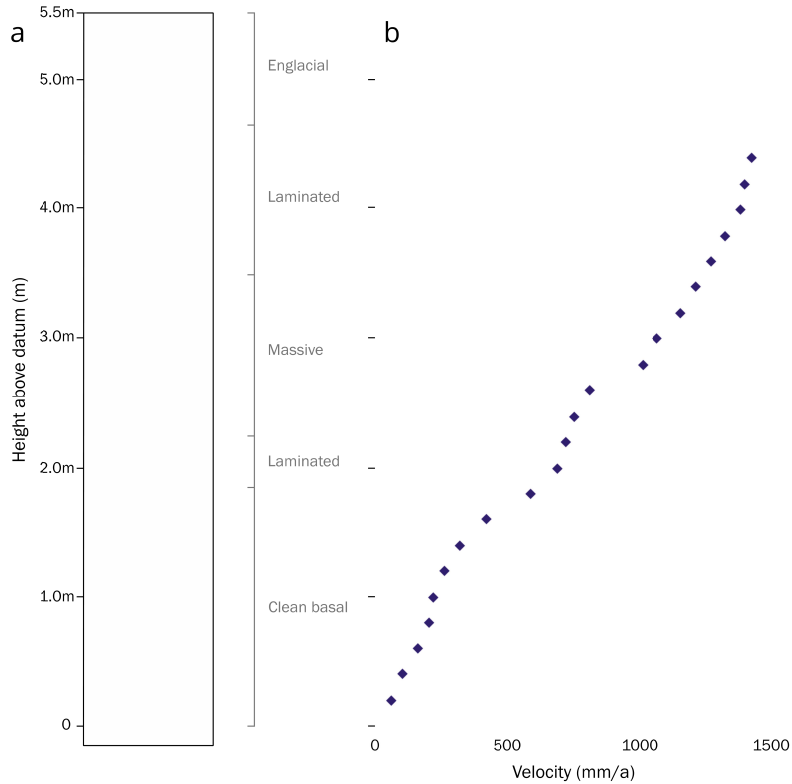
349 3.4 Ice motion and strain

350 3.4.1 Velocity of ice in the tunnel

351 A plumbline was located on the right wall in the shaft excavated at the end of the tunnel
 352 (Figure 1) which spanned the 4.5 m section of the basal zone (Figure 8). Prominent offsets occur
 353 in the displacement profile at 1.7 and 2. m above the measurement datum. The offset 1.7 m
 354 above the datum is 74 mm.a⁻¹ and the one located at 2.7 m is 130 mm.a⁻¹. Both the offsets occur
 355 between pegs that were 100 mm apart at the boundaries the laminated and massive subfacies.
 356 Displacements at the 1.7 m interface were also measured directly using engineers dial gauges
 357 rock-bolted onto cobbles and boulders embedded massive subfacies but protruding into the
 358 laminated subfacies. At the four locations measurements made over a period 4 to 31 days the
 359 displacements ranged between 46 and to 167 mm.a⁻¹.

360

361



362

363 **Figure 8.** (a) Stratigraphic log of the shaft excavated at the end of the tunnel, showing clean
 364 glacier ice underlain by stratified ice consisting of laminated and massive subfacies. Granite
 365 boulders in the ice have lee and stoss-side air filled cavities shown as black zones. (b) Velocity
 366 measured with a plumbline surveyed episodically up to 403 days after installation. The two steps
 367 in the profile at 1.7 and 2.7 m above the datum occur at the interfaces between the massive and
 368 laminated subfacies facies.
 369

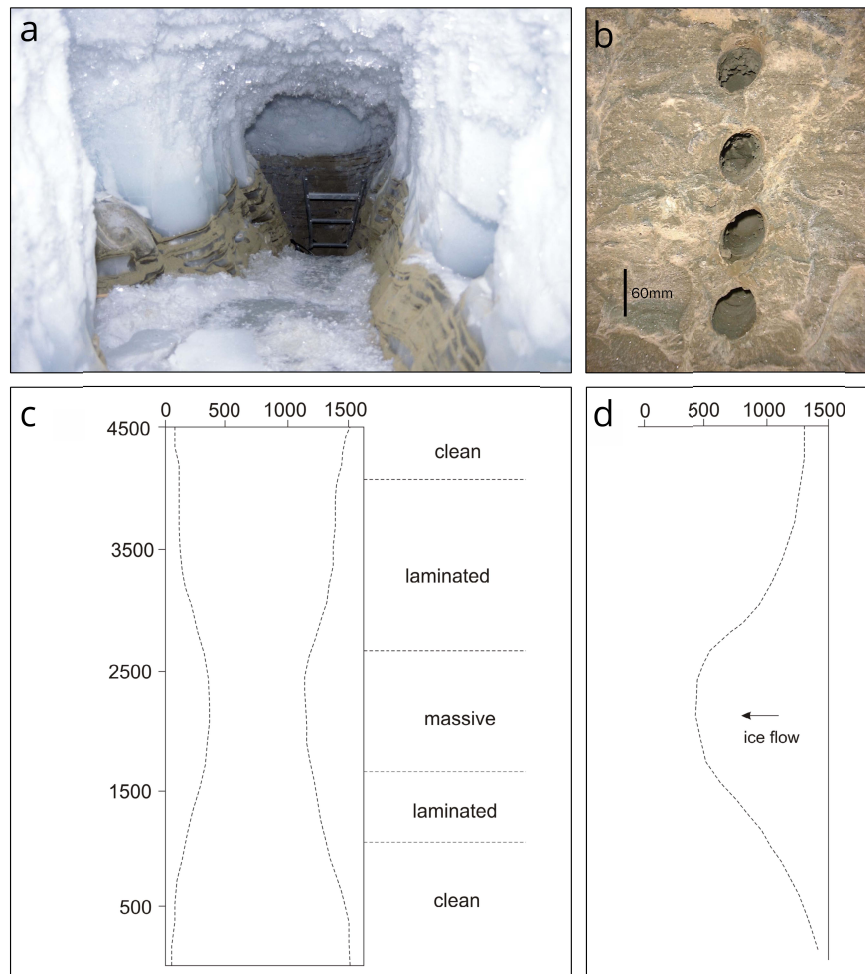
370 3.4.2 Velocity of ice at the glacier surface

371 Optically surveyed velocity measurements between 2.1 m.a^{-1} close to the ice margin to
 372 5.5 m.a^{-1} in the glacier center line over 376 and 769 days (Figure 1). The surface velocity close
 373 to the tunnel was 2.1 m.a^{-1} , which is within the error of a 2.5 m.a^{-1} , velocity determined by
 374 optical surveying of pegs placed in the cliff (B. Hubbard pers. comm. 2007). These velocity
 375 measurements are very similar to the magnitude and pattern of surface velocities determined by
 376 GPS surveying of stakes on the glacier surface (Pettit et al., 2014).
 377

378 3.4.3 Strain of ice in the basal ice shaft

379 The highest shear strain rates are in the massive subfacies followed by the laminated
 380 subfacies and the englacial ice (Figure 6d). These differences align with observations made of
 381 tunnel closure and deformation of boreholes and strain markers cut into the tunnel walls. After
 382 403 days the greatest deformation of the tunnel occurred in the shaft excavated at the end of the
 383 tunnel where the rectangular cross section of the tunnel was observed to deform into a keyhole

384 shape (Figure 9a). Cylindrical holes cut in the tunnel walls with a diamond corer deformed
 385 rapidly in the laminated subfacies during the experiment (Figure 9b). Within 4 days the holes
 386 deformed into ellipses with axial ratios between 1.38 and 1.53, whereas corresponding holes in
 387 the low debris concentration laminated subfacies had average axial ratios of 1.2. There was no
 388 detectable deformation of the holes in clean ice. Closure occurred fastest at the interface between
 389 the laminated subfacies above and below the massive subfacies layer (Figure 9c). Bulging also
 390 occurred in the back wall of the tunnel which was oriented transverse to ice flow (Figure 1). Here
 391 the maximum rates of deformation occurred in the laminated subfacies and the bulging
 392 resembled the shape of a plug (Figure 9d).
 393



394

395 **Figure 9.** Evidence of the differential and localized deformation in the tunnel. (a) Photograph of
 396 the end of the tunnel 403 days after excavation. The walls of the shaft were originally planar and
 397 vertical. Most of the closure has occurred at the interface between the laminated and massive
 398 subfacies in the lower part of the photograph. The end of the ladder is 600 mm wide. (b) Closure
 399 of 59 mm diameter core holes in the massive subfacies 4 days after the samples were cored. (c)
 400 Closure of the cross section of the shaft excavated at the end of the tunnel 403 days after
 401 excavation. (d) Bulging of the rear wall of the tunnel surveyed 403 days after excavation.

402 4 Discussion

403 4.1 Motion in basal ice layer

404 The measurements made in the tunnel show that deformation is dominated by progressive
405 simple shear within the debris bearing ice with strong differences in the rate of deformation in
406 different ice facies. The highest rates of strain occur in the massive subfacies followed by the
407 laminated subfacies and the englacial facies, a pattern that is the same order as the direct shear
408 tests. Two exceptions to the pattern of progressive simple shear are the presence of offsets in the
409 plumbline profile which maybe thin shear zone or sliding interfaces and the presence of
410 polyharmonic recumbent folds which point to flow perturbations within the basal ice.

411 The offsets in the velocity profile recorded at 1.7 and 2.7 m above the datum occur at
412 interfaces between the massive and laminated subfacies (Figure 8). Measurements of
413 displacements on boulders at the upper interface, together with the development of air-filled
414 cavities and slickensides suggest there may be sliding at these interfaces. However, the spacing
415 of the measurement pegs used in the plumbline (100 mm) preclude a definitive interpretation.
416 The offsets could be produced by sliding or by narrow zones of higher rates of shear. Shear
417 localization is also a feature of some triaxial tests (Figure 7). The possibility of sliding is
418 discussed in section 6.2.

419 The deformation structures observed around particles in the laminated subfacies (Figure
420 6a) suggest a sense of vorticity (Samyn et al., 2009), and the pebbles appear very similar to
421 sigma grains observed in deformed geological materials (Passchier & Simpson, 1986). Tight,
422 recumbent, polyharmonic folds are common, particularly at the interfaces between the laminated
423 facies and the massive facies (Figure 6c). Short wavelength parasitic folds that occur at the axes
424 of the large folds are sheared in the direction of flow (Figure 6c). Such recumbent polyharmonic
425 folds typically form in shear zones where instabilities develop at the boundaries of adjacent
426 layers with different viscosities (Ramsay & Huber, 1987). This interpretation is consistent with
427 our observations of folding at the interfaces between the laminated subfacies and the englacial
428 ice and within the laminated subfacies where clean clear ice is interbedded with debris-bearing
429 ice (Figure 4). The recumbent geometry of the folds together with the presence of numerous
430 parasitic folds that appear to be sheared at the fold hinges (Figure 6c) suggests a sinistral rotation
431 of objects in the basal ice (i.e. anticlockwise) and progressively attenuation that results in the
432 pervasive laminar structure of the basal zone. In the predominantly compressive flow regime that
433 characterizes the glacier margin the formation of folds leads to shortening and thickening of the
434 basal layer.

435 A further source of instability in the basal zone are perturbations associated with pebble
436 to boulder-sized particles that occur throughout the basal ice. Since these particles rest in a
437 deforming medium in which deformation increases from bottom to top, the particles bridge a
438 velocity gradient which results in sinistral rotation. In shear zones rotation occurs at a rate that
439 can be significantly lower than the instantaneous shear strain rate (Simpson and De Paor, 1993).
440 The combination of rotation of the particles and ice flowing over their upper surfaces has led to
441 the development of morphologies similar to sigma grains in other geological materials. These
442 particles are characterized by coatings of fine particles, striae in multiple directions, and pressure
443 shadows at the stoss and lee sides of the grains. In the case of particles >10 mm in diameter, air-

444 filled cavities have developed adjacent to the clasts. (Figure 6b). Cavities on the margins of
445 boulder-sized particles were characterized by grooved linear markings on the cavity roofs. These
446 features resemble slickenslides in deformed rocks where polished and striated surfaces result
447 from friction produced at fault surfaces. The slickenslides are a series of grooves which are
448 impressions of the asperities of the particles that the ice has flowed over. Some of these cavities
449 degassed when punctured, i.e. the gas was above atmospheric pressure. Such cavities have also
450 been in the base of Suess Glacier, a small cold-based alpine glacier located about 12 km east of
451 Taylor Glacier (Fitzsimons et al., 2000).

452 Thin sections of small clasts (<10 mm) from the laminated subfacies show that the
453 pressure shadows consist of clear ice, which may be the product of recrystallization (Samyn et
454 al., 2005a). Ribbons of fine, elongated ice crystals at the boundaries of debris-bearing and clear
455 laminae identified in microstructural analysis occur where with the relative motion between ice
456 and particles being achieved by slip across low-viscosity interfacial water films (Samyn et al.,
457 2008). In addition, at the interface between the debris-rich and the clean ice layers of the
458 laminated subfacies, the ice crystals show clear signs of dynamic recrystallization and
459 differential strain. These patterns are indicative of the high rates of distributed shear and
460 relatively low strength of the in the debris-bearing facies identified in section 3.3.

461 4.2 Is sliding at -18°C plausible?

462 The two offsets in the velocity profile amount to 204 mm.a^{-1} (130 mm at 2.7 m and 74
463 mm at 1.7 m above datum, Figure 8), which corresponds to 14% of motion within the basal zone
464 and about 8% of glacier motion at the ice edge (using 2.5 m.a^{-1} as the ice edge surface velocity).
465 Taken together with the short-term point measurements of displacement above boulders and the
466 presence of cavities and slickenslides, these observations suggest two possibilities: sliding or
467 rapid deformation in thin (<100 mm) zones.

468 There is both theoretical and field evidence for sliding at subfreezing temperatures.
469 Gilpin (1979) argued for the existence of liquid-like layers between the ice and the substrate,
470 which led Shreeve (1984) and Fowler (1986) to suggest that sliding is possible at subfreezing
471 temperatures. Subsequently sliding has been observed or inferred at temperatures ranging
472 between -1 and -17°C in several glaciers (Echelmeyer & Zhongxiang, 1987; Cuffey et al., 1999;
473 Fitzsimons et al., 2000). In Meserve Glacier a small alpine glacier in the Dry Valleys with a
474 basal temperature of -17°C displacement measurements at the ice boundary layer over boulders
475 led Cuffey et al. (1999) to conclude that ice was sliding over the boulders at velocities between 2
476 and 8 mm.a⁻¹, which was ten times greater than the local strain rate. The sliding was associated
477 with lee cavities on boulders which carried slickensides like the ones described in this study.
478 Cuffey et al. attributed the sliding at these low temperatures to the presence of interfacial films.
479 Our point measurements on boulders range from 46 to 167 mm.a⁻¹ and the two offsets in the
480 vertical profile at the upper and lower boundaries of the massive subfacies are 130 and 74 mm.a⁻¹
481 respectively. If these displacements are from sliding, as seems likely, the velocities are more than
482 an order of magnitude greater than those observed at Meserve Glacier at the same temperature.
483 An important difference between the two sites is that the suspended sediment and solute
484 concentrations in the basal ice at Taylor Glacier are considerably higher than in Meserve Glacier
485 (Holdsworth, 1974; Samyn et al., 2005b). The ice is around 20 m thick at both locations.

486 The theory of premelting describes the formation and existence of liquid at temperatures
487 below the solid region in a bulk phase diagram (Wettlaufer, 1999) and provides a useful
488 theoretical context for field observations of subfreezing sliding. Surface premelting refers to the
489 process in which a liquid or a liquid-like film is present at the surface of a crystal in contact with
490 its vapor phase below the bulk freezing point, or at the junctions of crystals of the same material
491 (Wettlaufer, 1999). The thickness of liquid films is extremely sensitive to the concentrations of
492 solutes (Wettlaufer, 1999), and potentially to the nature of debris entrained within the ice (Dash
493 et al., 1995). In Taylor Glacier the average total dissolved solids in the laminated and massive
494 subfacies are two and three orders of magnitude greater respectively than that of the englacial
495 ice. It is likely that the solute values are conservative because our samples were 10 mm wide and
496 100 mm long and provide average values through multiple laminae.

497 The high sediment concentrations in the massive subfacies together with the large
498 component of fine sand and silt may also be conducive to sliding because finer-grained
499 sediments are associated with depressed freezing points because the curvature of the water
500 interfaces is greater. An experimental study of sliding behaviour by Emerson and Rempel (2007)
501 pointed to particle size and concentration controls on sliding behaviour. They distinguish a
502 “sandy” regime in which there is relatively high resistance to sliding associated with higher
503 debris concentration and larger particle sizes. By contrast, when debris concentrations are lower
504 and particle sizes are smaller there is an abrupt transition into a “slippery” regime in which shear
505 resistance is no longer dependent on normal load. The physical characteristics of the debris-rich
506 basal ice in Taylor Glacier together with the high solute concentrations (Table 2) and presence of
507 fine-grained particles (Figure 8) seems to be compatible with larger volumes of premelted liquid
508 and lower friction. Further evidence for the presence of premelted liquid in the basal ice of
509 Taylor Glacier was provided by Samyn et al. (2005a) who suggested that subtle changes in the
510 gas composition were typical of phase changes involving minute quantities of water and
511 crystallographic evidence of lattice loosening indicate small-scale strain variations that are
512 compatible with slight changes in water content.

513 4.3 Origin and evolution of the basal zone

514 The basal ice facies observed in tunnels in Taylor Glacier bear some striking similarities
515 to the model of basal ice formation under freezing conditions proposed by Christoffersen et al.
516 (2006). These authors developed a numerical model for basal ice formation based on the ratio of
517 the supply of subglacial water to the freezing rate in which the following types of ice are
518 produced depending on the subglacial hydrology: clear ice is produced when water is freely
519 available; laminated ice if the supply of water is constrained; massive ice if the water supply is
520 further constrained; and a solid facies if meltwater is depleted and there is rapid freezing. The
521 massive subfacies observed beneath Taylor Glacier is structurally very similar to the modelled
522 massive facies because it consists of finely stacked laminae that appear to be massive from visual
523 observation (Figure 4 c and d). A regelation origin for the massive and laminated subfacies is
524 consistent with many lines of evidence for the presence of liquid water beneath Taylor Glacier
525 (Hubbard et al., 2004; Mikucki et al., 2015; Badgeley et al., 2017; Lyons et al., 2019) and with
526 cooling of the base of the glacier as it thins toward the margin.

527 A significant difference with these regelation model proposed by Christoffersen et al.
528 (2006) is that the Taylor Glacier basal ice layer consists of the debris bearing ice interbedded
529 with clean bubbly englacial ice. This interbedding together with abundant evidence of sinistral
530 rotation described above, the presence of recumbent folds and the development of parasitic folds
531 suggests that tectonic processes play a role in basal ice formation. The occurrence of tight
532 recumbent folds in the laminated subfacies (Figure 6c) and the interbedded nature of the
533 laminated subfacies with the englacial facies suggests that debris bearing-ice is being mixed with
534 adjacent relatively clean ice. Such mixing is to be expected at structural boundaries where there
535 are rheological contrasts, an association that is well known to lead to flow perturbations in shear
536 zones (Ramsay & Huber, 1987; Passchier & Simpson, 1986). These perturbations first lead to
537 basal zone thickening, then to shortening and stretching. Because of the pervasive simple shear
538 in the basal zone the folds are likely to be rapidly attenuated into the planar structures that
539 characterize the bulk of ice in the basal zone. From the observed deformation structures together
540 with the patterns of deformation we conclude that there is tectonic evolution of the basal ice
541 along the flow path toward the glacier margin. We suggest that the laminated subfacies is at least
542 partly a tectonic facies that is derived from mechanical deformation at the upper and lower
543 boundaries of the massive subfacies. This tectonic origin is further supported by gas
544 chromatography (Samyn et al., 2005a) and water co-isotopic measurements (Souchez et al.,
545 2004), both conducted at the cm-scale within the basal ice zone, showing that the clean and
546 debris-bearing ice layers from the laminated subfacies present a ‘meteoric’ signature, thereby
547 precluding their origin as resulting from macro-scale regelation process.

548 The tunnel walls show that the basal ice layers rise toward the ice margin and that at
549 some locations there is an abrupt termination of the basal debris layers before the ice cliff (Figure
550 2). This termination appears to be the product of partial overriding and entrainment of the ice apron
551 that forms at the foot of the terminal cliff in places. The process of apron entrainment has been
552 described by Shaw (1977) and Fitzsimons et al. (2008).

553 4.4 Implications for glacier behaviour

554 Displacements measured in the tunnel show that the basal zone contributes about 1.5 m
555 of motion per year which is about 60% of the 2.5 m.a^{-1} surface velocity at the ice edge. The same
556 value of basal motion was observed in “ice-laden drift” with a temperature of -4°C in Urumqi
557 No 1 Glacier (Echelmeyer & Zhongxiang, 1987). Similar results have also been reported from
558 Russell Glacier, a polythermal outlet glacier from Greenland where 16% of the motion was
559 attributed to deformation of basal ice (Waller & Hart, 1999). At Taylor Glacier a previous study
560 (Petit et al., 2014) used a two-layer flow model to predict the basal properties of Taylor Glacier
561 and concluded that deformation of the basal ice layer accounted for 85 to 98% of glacier motion,
562 that the basal ice layer was likely 10-15 m thick, and that the basal ice was 20-40 times softer
563 than clean englacial ice. While the measurements made in the tunnel are broadly consistent with
564 the argument that the basal ice layer plays a significant role in the behaviour of Taylor Glacier,
565 the basal ice layer that we have characterized is thinner, does not account for such a large
566 proportion of surface motion and is only 2 times softer than the values concluded by Pettit et al.
567 (2014).

568 One of the issues in examining the behaviour of ice and debris at the base of glaciers is
569 that there is a continuum between debris-rich basal ice and ice-rich debris that might form the
570 bed of a glacier. What one researcher might describe as basal ice another might describe as ice-
571 rich sediment or frozen till. This problem is exacerbated when observations are made using bore
572 holes because of uncertainties concerning the location of the glacier bed and because the holes
573 cannot penetrate coarse sediment, unless local conditions allow diamond drilling equipment to be
574 deployed (e.g. Truffer et al., 2000). For example, work by Echelmeyer and Zhongxiang (1987) is
575 widely cited as evidence for subglacial deformation in subfreezing conditions. However, their
576 description of the contact between the glacier bed and the substrate as a junction between clear
577 glacier ice with a low debris content and the bed samples of which contain 21-39% debris. In
578 Taylor Glacier such a boundary occurs between the englacial ice and the laminated subfacies,
579 which is contained entirely within the debris-bearing basal ice. Although the tunnel-based
580 observations at Taylor Glacier leave little doubt that the measurements have been made within
581 the basal ice layer (Figure 4), it is clear that the displacement profile measured through the basal
582 zone resembles that of a subglacial sediment deformation profile (e.g. Boulton & Hindmarsh,
583 1987; Boulton, 2006) because the strain is heterogenous and the velocity profiles are stepped
584 because of the presence of offsets which appear to be due to sliding. The observations made in
585 the tunnels support the view that the base of glaciers should be defined as a zone, not a single
586 zero-velocity boundary at a simple ice-substrate interface (Waller, 2001, Fitzsimons, 2006; Pettit
587 et al., 2014).

588 4.5. Implications for glacial geology

589 Our measurements show that the basal zone has an emergence velocity of around 1.5 m a^{-1} ,
590 i.e. the velocity at which it arrives at the ice edge. The average debris concentration through
591 massive subfacies is 26% by volume for a 1.2 m-thick layer and for the laminated subfacies is
592 12% vol. for 1.6 m-thick layer which together yields $0.5 \text{ m}^3 \cdot \text{a}^{-1}$ of debris per 1 m of ice margin
593 per year. These estimates are half the estimate made by Pettit et al. (2014). The difference in our
594 calculations are that the emergence velocity is lower, the thickness of the basal layers
595 substantially smaller (4.5 m vs. 10 m) although the measured debris concentrations in the basal
596 ice are much greater than those suggested by Pettit et al. (2014). The volume of debris that is
597 discharged to the ice margin is not consistent with the modest accumulations of material that has

598 accumulated along the ice edge and absence of moraines (Figure 1). There are no substantial
599 accumulations of material at the ice margin because fluvial processes rapidly remove most of the
600 debris that that is discharged from the ice cliff. A steep ephemeral marginal meltwater stream,
601 Santa Fe Creek, is pinned against the ice margin by the adverse slope adjacent to the ice edge
602 (Figure 1). Consequently all the fine-grained sediment excavated from the basal zone was
603 removed and transported into Lake Bonney within one year of the excavations. A boulder and
604 cobble lag was all that remained. An exception to this process is the small ice cored moraine that
605 rests on the delta of Santa Fe Creek adjacent to Blood Falls at the glacier terminus. Basal ice is
606 preserved in the core of this moraine, and ablation of the ice has produced a silty till with
607 numerous faceted and striated clasts. This material is indistinguishable from the basal ice
608 observed in the tunnels.

609 A combination of high debris concentrations in the debris-bearing ice and the high shear
610 experienced within the ice has produced faceted and abraded clasts and a high proportion of silt-
611 sized particles in particle size distributions. These characteristics are similar to the sedimentary
612 signature of temperate glacial environments which are dominated by high rates of abrasion and
613 contrast strongly with the sedimentary signature of cold-based glaciers which are dominated by
614 sandy gravel, glaciectonically deformed permafrost and aeolian deposits (Hambrey &
615 Fitzsimons, 2010; Hambrey & Glasser, 2012; Fitzsimons & Howarth, 2020). These observations
616 highlight the complexity of basal ice processes at the margin of Taylor Glacier and that simple
617 sedimentological criteria may not always be a sound basis for reconstructing glaciers with
618 different thermal regimes.

619 **5 Conclusions**

620 The basal zone of Taylor Glacier is characterized by a complex strain distribution that
621 results from heterogeneous deformation within the basal zone. The strongest materials and
622 lowest rates of deformation occur in ice layers with low debris concentrations and the weakest
623 materials and highest rates of deformation occur in layers of ice with the highest debris
624 concentrations and high solute loads. Ice with a laminated appearance has an intermediate
625 strength.

626 Deformation of the whole basal zone accounts for 60% of glacier motion at this ice
627 marginal location. Velocity profiles determined using plumbines suggest that either the ice is
628 sliding at structural interfaces or that high rates of shear are localized to in narrow (<100 mm)
629 zones accounting for 14% of glacier motion. Short term measurement of displacements using
630 engineers dial gauges together with the development of cavities and slickenslides in the ice
631 support the interpretation of sliding of up to 167 mm.a^{-1} or very localized interfacial flow despite
632 the low basal temperature (-18°C). These observations are consistent with studies of ice
633 crystallography which show that evidence of pervasive shearing and strain localization at
634 sedimentological and structural interfaces (Samyn et al., 2008).

635 Heterogeneous deformation results in flow perturbations which cause folding which
636 drives mixing within the basal zone which results in blending of debris-bearing and clean ice
637 facies. Mixing of adjacent ice facies results in tectonic evolution of the basal ice along the flow
638 line together with basal zone thickening toward the margin of the glacier. Deformation

639 measurements together with observations of folding and shearing suggest that at least part of the
640 laminated subfacies has been produced by mechanical deformation within the basal zone.

641 High rates of strain combined with high debris concentrations in the debris-bearing ice
642 produce a high abrasion environment which is consistent with abundant heavily faceted and
643 striated clasts and a strong silt mode in particle size distributions. The combination of the
644 sedimentary signature of the abraded and faceted particles, the production of high volumes of
645 silt-sized particles and the relatively high sediment flux of the basal zone are characteristics
646 normally associated with temperate glaciers. However, the structural and geochemical signature
647 of the basal profile reflects the cold nature of the marginal ice.

648 Finally, our observation of the structure, composition and deformation of basal ice in
649 Taylor Glacier support the view that glacier beds are zones in which deformation is spatially and
650 temporally variable. Our observations and measurements show that the glacier bed is not as a
651 single zero-velocity boundary further suggest that glacier flow models need to incorporate
652 rheologically distinct layers to capture spatially variable behaviour of debris bearing basal ice
653 (e.g. Petit et al., 2014).

654 **Acknowledgments**

655 This work was supported by the Marsden Fund, Royal Society of NZ grant “Direct observations of basal
656 ice and substrate deformation at subfreezing temperatures”. The University of Otago and the Belgian
657 Antarctic Programme also supported the work and logistical support was provided by Antarctica New
658 Zealand to Event K064. We thank Dr. Kevin McManus, formerly of the Department of Civil Engineering,
659 University of Canterbury for providing the direct shear device and modifying it for use in the tunnel. We
660 are grateful for field assistance provided by Marcus Vandergoes, Mike Hambrey, Paul Sirota, Tracey
661 Morgan, Vaughn Filmer and Katrin Rohl. Chris Garden designed and drew the diagrams.

662 **Open Research**

663 The data collected during the field study together with video clips of the excavation and additional
664 photographs of the tunnels and basal ice are available at <https://doi.org/10.5281/zenodo.8232003>
665 (Fitzsimons, 2023).

666 **References**

667 Alley, R. B., Cuffey, K. M., Evenson, E. B., Strasser, J. C., Lawson, D. E., & Larson, G. J.
668 (1997). How glaciers entrain and transport basal sediment: Physical constraints.
669 *Quaternary Science Reviews*, 16(9), 1017–1038. [https://doi.org/10.1016/s0277-](https://doi.org/10.1016/s0277-3791(97)00034-6)
670 [3791\(97\)00034-6](https://doi.org/10.1016/s0277-3791(97)00034-6)

671
672 Alley, R. B., Cuffey, K. M., & Zoet, L. K. (2019). Glacial erosion: status and outlook. *Annals of*
673 *Glaciology*, 60(80), 1–13. <https://doi.org/10.1017/aog.2019.38>

674
675 Astakhov, V. I., Kaplyanskaya, F. A., & Tarnogradsky, V. D. (1996). Pleistocene permafrost of
676 West Siberia as a deformable glacier bed. *Permafrost and Periglacial Processes*, 7(2),

- 677 165–191. [https://doi.org/10.1002/\(sici\)1099-1530\(199604\)7:2<165::aid-](https://doi.org/10.1002/(sici)1099-1530(199604)7:2<165::aid-ppp218>3.0.co;2-s)
678 [ppp218>3.0.co;2-s](https://doi.org/10.1002/(sici)1099-1530(199604)7:2<165::aid-ppp218>3.0.co;2-s)
679
- 680 Badgeley, J. A., Pettit, E. C., Carr, C. G., Tulaczyk, S., Mikucki, J. A., & Lyons, W. B. (2017).
681 An englacial hydrologic system of brine within a cold glacier: Blood Falls, McMurdo
682 Dry Valleys, Antarctica. *Journal of Glaciology*, 63(239), 387–400.
683 <https://doi.org/10.1017/jog.2017.16>
684
- 685 Boulton, G. S. (2006). Glaciers and their Coupling with Hydraulic and Sedimentary Processes.
686 *Glacier Science and Environmental Change*, 2–22.
687 <https://doi.org/10.1002/9780470750636.ch2>
688
- 689 Boulton, G. S., & Hindmarsh, R. C. A. (1987). Sediment deformation beneath glaciers: Rheology
690 and geological consequences. *Journal of Geophysical Research*, 92(B9), 9059.
691 <https://doi.org/10.1029/jb092ib09p09059>
692
- 693 Christoffersen, P., Tulaczyk, S., Carsey, F. D., & Behar, A. E. (2006). A quantitative framework
694 for interpretation of basal ice facies formed by ice accretion over subglacial sediment.
695 *Journal of Geophysical Research*, 111(F1). <https://doi.org/10.1029/2005jf000363>
696
- 697 Clarke, G. K. C. (2005). Subglacial Processes. *Annual Review of Earth and Planetary Sciences*,
698 33(1), 247–276. <https://doi.org/10.1146/annurev.earth.33.092203.122621>
699
- 700 Cohen, D. (2000), Rheology of ice at the bed of Engabreen, Norway, *J. Glaciol.*, 46(155), 611–
701 621. <https://doi:10.3189/172756500781832620>
702
- 703 Cuffey, K. M., Conway, H., Hallet, B., Gades, A. M., & Raymond, C. F. (1999). Interfacial
704 water in polar glaciers and glacier sliding at -17°C . *Geophysical Research Letters*, 26(6),
705 751–754. <https://doi.org/10.1029/1999gl900096>
706
- 707 Cuffey, K. M., Conway, H., Gades, A., Hallet, B., Raymond, C. F., & Whitlow, S. (2000).
708 Deformation properties of subfreezing glacier ice: Role of crystal size, chemical
709 impurities, and rock particles inferred from in situ measurements. *Journal of Geophysical*
710 *Research: Solid Earth*, 105(B12), 27895–27915. <https://doi.org/10.1029/2000jb900271>
711
- 712 Dash, J. G., Fu, H., & Wettlaufer, J. S. (1995). The premelting of ice and its environmental
713 consequences. *Reports on Progress in Physics*, 58(1), 115–167.
714 <https://doi.org/10.1088/0034-4885/58/1/003>

715

716 Dash, J. G., Rempel, A. W., & Wettlaufer, J. S. (2006). The physics of premelted ice and its
717 geophysical consequences. *Reviews of Modern Physics*, 78(3), 695–741.
718 <https://doi.org/10.1103/revmodphys.78.695>

719

720 Echelmeyer, K., & Zhongxiang, W. (1987). Direct Observation of Basal Sliding and
721 Deformation of Basal Drift at Sub-Freezing Temperatures. *Journal of Glaciology*,
722 33(113), 83–98. <https://doi.org/10.3189/s0022143000005396>

723

724 Emerson, L. F., & Rempel, A. W. (2007). Thresholds in the sliding resistance of simulated basal
725 ice. *The Cryosphere*, 1(1), 11–19. <https://doi.org/10.5194/tc-1-11-2007>

726

727 Fitzsimons, S. (2006). Mechanical Behaviour and Structure of the Debris-Rich Basal Ice Layer.
728 In *Glacier Science and Environmental Change* (pp. 329–335). Blackwell.
729 <https://doi.org/10.1002/9780470750636.ch65>

730

731 Sean Fitzsimons. (2023). Taylor Glacier Tunnel: Measurements of the composition, deformation
732 and strength of basal ice made in a tunnel in Taylor Glacier, Antarctica [Data set].
733 Zenodo. <https://doi.org/10.5281/zenodo.8232003>

734

735 Fitzsimons, S., & Howarth, J. (2020). Development of push moraines in deeply frozen sediment
736 adjacent to a cold-based glacier in the McMurdo Dry Valleys, Antarctica. *Earth Surface*
737 *Processes and Landforms*, 45(3), 622–637. <https://doi.org/10.1002/esp.4759>

738

739 Fitzsimons, S. J., McManus, K. J., & Lorrain, R. D. (1999). Structure and strength of basal ice
740 and substrate of a dry-based glacier: evidence for substrate deformation at sub-freezing
741 temperatures. *Annals of Glaciology*, 28, 236–240.
742 <https://doi.org/10.3189/172756499781821878>

743

744 Fitzsimons, S. J., Lorrain, R. D., & Vandergoes, M. J. (2000). Behaviour of subglacial sediment
745 and basal ice in a cold glacier. *Geological Society, London, Special Publications*, 176(1),
746 181–190. <https://doi.org/10.1144/gsl.sp.2000.176.01.14>

747

748 Fitzsimons, S. J., McManus, K. J., Sirota, P., & Lorrain, R. D. (2001). Direct shear tests of
749 materials from a cold glacier: implications for landform development. *Quaternary*
750 *International*, 86(1), 129–137. [https://doi.org/10.1016/s1040-6182\(01\)00055-6](https://doi.org/10.1016/s1040-6182(01)00055-6)

751

- 752 Fitzsimons, S., Webb, N., Mager, S., MacDonell, S., Lorrain, R., & Samyn, D. (2008).
753 Mechanisms of basal ice formation in polar glaciers: An evaluation of the apron
754 entrainment model. *Journal of Geophysical Research*, 113(F2).
755 <https://doi.org/10.1029/2006jf000698>
756
- 757 Fitzsimons, S., Sharp, M., & Lorrain, R. (2023). Subglacial deformation of permafrost beneath
758 Wright Lower Glacier, Antarctica as revealed by direct observations and measurements
759 from a subglacial tunnel. *Geomorphology*, 440, 108886.
760 <https://doi.org/10.1016/j.geomorph.2023.108886>
761
- 762 Foley, N., Tulaczyk, S., Auken, E., Schamper, C., Dugan, H., Mikucki, J., Virginia, R., & Doran,
763 P. (2016). Helicopter-borne transient electromagnetics in high-latitude environments: An
764 application in the McMurdo Dry Valleys, Antarctica. *Geophysics*, 81(1), WA87–WA99.
765 <https://doi.org/10.1190/geo2015-0186.1>
766
- 767 Fowler, A. C. (1986). Sub-Temperate Basal Sliding. *Journal of Glaciology*, 32(110), 3–5.
768 <https://doi.org/10.3189/s0022143000006808>
769
- 770 Gilpin, R. R. (1979). A model of the “liquid-like” layer between ice and a substrate with
771 applications to wire regelation and particle migration. *Journal of Colloid and Interface*
772 *Science*, 68(2), 235–251. [https://doi.org/10.1016/0021-9797\(79\)90277-7](https://doi.org/10.1016/0021-9797(79)90277-7)
773
- 774 Goughnour, R. R., & Andersland, O. B. (1968). Mechanical Properties of a Sand-Ice System.
775 *Journal of the Soil Mechanics and Foundations Division*, 94(4), 923–950.
776 <https://doi.org/10.1061/jsfeaq.0001179>
777
- 778 Hambrey, M. J., Milnes, A. G., & Siegenthaler, H. (1980). Dynamics and Structure of
779 Griesgletscher, Switzerland. *Journal of Glaciology*, 25(92), 215–228.
780 <https://doi.org/10.3189/s0022143000010455>
781
- 782 Hambrey, M. J., & Müller, F. (1978). Structures and Ice Deformation in the White Glacier, Axel
783 Heiberg Island, Northwest Territories, Canada. *Journal of Glaciology*, 20(82), 41–66.
784 <https://doi.org/10.3189/s0022143000021213>
785
- 786 Holdsworth, G. (1974). Meserve Glacier Wright Valley, Antarctica: Part I. Basal
787 Processes. Institute of Polar Studies Report No. 37, Ohio State University, Columbus,
788 Ohio.
789

- 790 Hubbard, B. (2006). On the Relationships Between Field Data and Numerical Models of Ice-
791 Mass Motion. *Glacier Science and Environmental Change*, 338–345.
792 <https://doi.org/10.1002/9780470750636.ch67>
793
- 794 Hubbard, B., Cook, S., & Coulson, H. (2009). Basal ice facies: a review and unifying approach.
795 *Quaternary Science Reviews*, 28(19–20), 1956–1969.
796 <https://doi.org/10.1016/j.quascirev.2009.03.005>
797
- 798 Hubbard, A., Lawson, W., Anderson, B., Hubbard, B., & Blatter, H. (2004). Evidence for
799 subglacial ponding across Taylor Glacier, Dry Valleys, Antarctica. *Annals of Glaciology*,
800 39, 79–84. <https://doi.org/10.3189/172756404781813970>
801
- 802 Hubbard, B., & Sharp, M. (1989). Basal ice formation and deformation: a review. *Progress in*
803 *Physical Geography: Earth and Environment*, 13(4), 529–558.
804 <https://doi.org/10.1177/030913338901300403>
805
- 806 Hubbard, B., & Sharp, M. (1993). Weertman regelation, multiple refreezing events and the
807 isotopic evolution of the basal ice layer. *Journal of Glaciology*, 39(132), 275–291.
808 <https://doi.org/10.3189/s002214300001594x>
809
- 810 Iverson, N. R. (2010). Shear resistance and continuity of subglacial till: hydrology rules. *Journal*
811 *of Glaciology*, 56(200), 1104–1114. <https://doi.org/10.3189/002214311796406220>
812
- 813 Jacka, T. H., Shavawn Donoghue, Li, J., William F. Budd, & Anderson, R. M. (2003).
814 Laboratory studies of the flow rates of debris-laden ice. *Annals of Glaciology*, 37, 108–
815 112. <https://doi.org/10.3189/172756403781815537>
816
- 817 Lawson, W. (1996). The relative strengths of debris-laden basal ice and clean glacier ice: some
818 evidence from Taylor Glacier, Antarctica. *Annals of Glaciology*, 23, 270–276.
819 <https://doi.org/10.3189/s0260305500013537>
820
- 821 Lyons, W. B., Mikucki, J. A., German, L. A., Welch, K. A., Welch, S. A., Gardner, C. B.,
822 Tulaczyk, S. M., Pettit, E. C., Kowalski, J., & Dachwald, B. (2019). The Geochemistry of
823 Englacial Brine From Taylor Glacier, Antarctica. *Journal of Geophysical Research:*
824 *Biogeosciences*, 124(3), 633–648. Portico. <https://doi.org/10.1029/2018jg004411>
825
- 826 Montross, S., Skidmore, M., Christner, B., Samyn, D., Tison, J.-L., Lorrain, R., Doyle, S., &
827 Fitzsimons, S. (2013). Debris-Rich Basal Ice as a Microbial Habitat, Taylor Glacier,

- 828 Antarctica. *Geomicrobiology Journal*, 31(1), 76–81.
829 <https://doi.org/10.1080/01490451.2013.811316>
830
- 831 Moore, P. L. (2014). Deformation of debris-ice mixtures. *Reviews of Geophysics*, 52(3), 435-
832 467.
833
- 834 Mikucki, J. A., Auken, E., Tulaczyk, S., Virginia, R. A., Schamper, C., Sørensen, K. I., Doran, P.
835 T., Dugan, H., & Foley, N. (2015). Deep groundwater and potential subsurface habitats
836 beneath an Antarctic dry valley. *Nature Communications*, 6(1).
837 <https://doi.org/10.1038/ncomms7831>
838
- 839 Nickling, W. G., & Bennett, L. (1984). The Shear Strength Characteristics of Frozen Coarse
840 Granular Debris. *Journal of Glaciology*, 30(106), 348–357.
841 <https://doi.org/10.1017/s0022143000006201>
842
- 843 Passchier, C. W., & Simpson, C. (1986). Porphyroclast systems as kinematic indicators. *Journal*
844 *of Structural Geology*, 8(8), 831–843. [https://doi.org/10.1016/0191-8141\(86\)90029-5](https://doi.org/10.1016/0191-8141(86)90029-5)
845
- 846 Pettit, E. C., Whorton, E. N., Waddington, E. D., & Sletten, R. S. (2014). Influence of debris-rich
847 basal ice on flow of a polar glacier. *Journal of Glaciology*, 60(223), 989–1006.
848 <https://doi.org/10.3189/2014jog13j161>
849
- 850 Powers, M. C. (1953). A New Roundness Scale for Sedimentary Particles. *SEPM Journal of*
851 *Sedimentary Research*, Vol. 23. [https://doi.org/10.1306/d4269567-2b26-11d7-](https://doi.org/10.1306/d4269567-2b26-11d7-8648000102c1865d)
852 [8648000102c1865d](https://doi.org/10.1306/d4269567-2b26-11d7-8648000102c1865d)
853
- 854 Ramsay, J. G., (1967). *Folding and Fracturing of Rocks*. McGraw Hill, New York. 568 pp.
855
- 856 Ramsay, J.G. & Huber, M. I. (1987). The techniques of modern structural geology. Folds and
857 Fractures, Vol. 2. Academic Press.
858
- 859 Rabus, B. T., & Echelmeyer, K. A. (1997). The flow of a polythermal glacier: McCall Glacier,
860 Alaska, U.S.A. *Journal of Glaciology*, 43(145), 522–536.
861 <https://doi.org/10.3189/s0022143000035139>
862
- 863 Rempel, A. W., Meyer, C. R., & Riverman, K. L. (2021). Melting temperature changes during
864 slip across subglacial cavities drive basal mass exchange. *Journal of Glaciology*, 68(267),
865 197–203. <https://doi.org/10.1017/jog.2021.107>

866

867 Robinson, P. H. (1984). Ice dynamics and thermal regime of Taylor Glacier, South Victoria
868 Land, Antarctica. *Journal of Glaciology*, 30(105), 153–160.
869 <https://doi.org/10.1017/S0022143000005888>

870

871 Samyn, D., Fitzsimons, S. J., & Lorrain, R. D. (2005a). Strain-induced phase changes within
872 cold basal ice from Taylor Glacier, Antarctica, indicated by textural and gas analyses.
873 *Journal of Glaciology*, 51(175), 611–619. <https://doi.org/10.3189/172756505781829098>

874

875 Samyn, D., Fitzsimons, S. J., & Lorrain, R. D. (2009). Rotating micro-structures in Antarctic
876 cold basal ice: implications for glacier flow and its interpretation. *International Journal*
877 *of Earth Sciences*, 99(8), 1849–1857. <https://doi.org/10.1007/s00531-009-0478-5>

878

879 Samyn, D., Svensson, A., & Fitzsimons, S. J. (2008). Dynamic implications of discontinuous
880 recrystallization in cold basal ice: Taylor Glacier, Antarctica. *Journal of Geophysical*
881 *Research*, 113(F3). <https://doi.org/10.1029/2006jf000600>

882

883 Samyn D., Svensson A., Fitzsimons S.J., & Lorrain R. (2005b). Ice crystal properties of amber
884 ice and strain enhancement at the base of cold Antarctic glaciers. *Annals of Glaciology*
885 40:185–190. <https://doi.org/10.3189/172756405781813618>

886

887 Sharp, M., Lawson, W., & Anderson, R. S. (1988). Tectonic processes in a surge-type glacier.
888 *Journal of Structural Geology*, 10(5), 499–515. [https://doi.org/10.1016/0191-
889 8141\(88\)90037-5](https://doi.org/10.1016/0191-8141(88)90037-5)

890

891 Shaw, J. (1977). Till body morphology and structure related to glacier flow. *Boreas*, 6(2), 189–
892 201. <https://doi.org/10.1111/j.1502-3885.1977.tb00348>

893

894 Shreve, R. L. (1984). Glacier Sliding at Subfreezing Temperatures. *Journal of Glaciology*,
895 30(106), 341–347. <https://doi.org/10.3189/s0022143000006195>

896

897 Simpson, C., & De Paor, D. G. (1993). Strain and kinematic analysis in general shear zones.
898 *Journal of Structural Geology*, 15(1), 1–20. [https://doi.org/10.1016/0191-
899 8141\(93\)90075-1](https://doi.org/10.1016/0191-8141(93)90075-1)

900

901 Souchez, R., Samyn, D., Lorrain, R., Pattyn, F. & Fitzsimons, S. (2004). An isotopic model for
902 basal freeze-on associated with subglacial upward flow of pore water. *Geophys. Res. Lett.*
903 31:L02401. <https://doi.org/10.1029/2003GL018861>

904

905 Thompson, A. C., Iverson, N. R., & Zoet, L. K. (2020). Controls on Subglacial Rock Friction:
906 Experiments With Debris in Temperate Ice. *Journal of Geophysical Research: Earth*
907 *Surface*, 125(10). <https://doi.org/10.1029/2020jf005718>

908

909 Truffer, M., Harrison, W. D., & Echelmeyer, K. A. (2000). Glacier motion dominated by
910 processes deep in underlying till. *Journal of Glaciology*, 46(153), 213–221.
911 <https://doi.org/10.3189/172756500781832909>

912

913 Waller, R. I. (2001). The influence of basal processes on the dynamic behaviour of cold-based
914 glaciers. *Quaternary International*, 86(1), 117–128. [https://doi.org/10.1016/s1040-](https://doi.org/10.1016/s1040-6182(01)00054-4)
915 [6182\(01\)00054-4](https://doi.org/10.1016/s1040-6182(01)00054-4)

916

917 Waller, R.I. & Hart, J.K.. (1999). Mechanisms and patterns of motion associated with the basal
918 zone of the Russell Glacier, south-west Greenland. *Journal of Glacial Geology and*
919 *Geomorphology*, 21, 1–20.

920

921 Waller, R. I., Murton, J. B., & Kristensen, L. (2012). Glacier–permafrost interactions: Processes,
922 products and glaciological implications. *Sedimentary Geology*, 255–256, 1–28.
923 <https://doi.org/10.1016/j.sedgeo.2012.02.005>

924

925 Warbritton, M. J., Iverson, N. R., Lacroix, F., and Schomacker, A. (2020). Strain patterns in
926 glacitectonically thrustsediments and conditions during thrusting. *Journal of*
927 *Structural Geology*, 137, 104064. <https://doi.org/10.1016/j.jsg.2020.104064>

928

929 Wettlaufer, J. S. (1999). Impurity Effects in the Premelting of Ice. *Physical Review Letters*,
930 82(12), 2516–2519. <https://doi.org/10.1103/physrevlett.82.2516>

931

932 Wettlaufer, J. S., Worster, M. G., Wilen, L. A., & Dash, J. G. (1996). A Theory of Premelting
933 Dynamics for all Power Law Forces. *Physical Review Letters*, 76(19), 3602–3605.
934 <https://doi.org/10.1103/physrevlett.76.3602>